

1 **Image-domain wavefield tomography with extended**
2 **common-image-point gathers**

3 **Tongning Yang**

4 **Formerly Center for Wave Phenomena, Colorado School of Mines**

5 **Presently BP America**

6 **Paul Sava**

7 **Center for Wave Phenomena, Colorado School of Mines**

8 (June 14, 2014)

9 Running head: **Image-domain wavefield tomography**

ABSTRACT

10 Waveform inversion is a velocity-model-building technique based on full waveforms as the input
11 and seismic wavefields as the information carrier. Conventional waveform inversion is implemented
12 in the data-domain. However, similar techniques referred to as image-domain wavefield tomography
13 can be formulated in the image domain and use a seismic image as the input and seismic wavefields
14 as the information carrier. The objective function for the image-domain approach is designed to
15 optimize the coherency of reflections in extended common-image gathers. The function applies a
16 penalty operator to the gathers, thus highlighting image inaccuracies arising from the velocity model
17 error. Minimizing the objective function optimizes the model and improves the image quality. The
18 gradient of the objective function is computed using the adjoint-state method in a way similar to that
19 in the analogous data-domain implementation. We propose an image-domain velocity-model build-
20 ing method using extended common-image-point space- and time-lag gathers constructed sparsely

21 at reflections in the image. The gathers moreover are effective in reconstructing the velocity model
22 in complex geologic environments and can be used as an economical replacement for conventional
23 common-image gathers in wave-equation tomography. A test on the Marmousi model illustrates
24 successful updating of the velocity model using common-image point gathers and resulting im-
25 proved image quality.

INTRODUCTION

26 Building an accurate and reliable velocity model remains a challenge in current seismic imaging
27 practice. In complex subsurface regions, prestack wave-equation depth migration (e.g., one-way
28 wave-equation migration or reverse-time migration) is a powerful tool for accurately imaging the
29 Earth's interior (Gray et al., 2001; Etgen et al., 2009). Because these migration methods are sensitive
30 to model errors, their widespread use significantly drives the need for high-quality velocity models
31 (Symes, 2008; Woodward et al., 2008; Virieux and Operto, 2009).

32 Waveform inversion represents a family of techniques for velocity model building using seismic
33 wavefields (Tarantola, 1984; Woodward, 1992; Pratt, 1999; Sirgue and Pratt, 2004; Plessix, 2006;
34 Vigh and Starr, 2008a; Plessix, 2009; Symes, 2009). This type of methodology, although usually
35 regarded as one of the costliest for velocity estimation, has been gaining momentum in recent years,
36 mainly because of its accuracy as well as advances in computing technology. Usually waveform
37 inversion is implemented in the data domain by adjusting the velocity model such that simulated
38 and recorded data match (Tarantola, 1984; Pratt, 1999). Such a data match problem often suffers
39 from cycle skipping due to an inaccurate initial model or missing low frequency in the data. (Warner
40 et al., 2013)

41 Velocity-model-building methods using seismic wavefields can be implemented in the image
42 domain. Instead of minimizing the data misfit, the techniques in this category update the velocity
43 model by optimizing the image quality. As stated by the semblance principle, the image quality
44 is optimized when the data are migrated with the correct velocity model (Al-Yahya, 1989). The
45 common idea is to optimize the coherency of reflection events in common-image gathers (CIGs)
46 via velocity-model-updating. These techniques are often referred as image-domain wavefield to-
47 mography. Unlike traditional ray-based reflection tomography methods, image-domain wavefield

48 tomography uses band-limited wavefields in the optimization procedure. Thus, this technique is
49 capable of handling complicated wave propagation phenomena such as multi-pathing in the sub-
50 surface. In addition, the band-limited character of the wave-equation engine more accurately ap-
51 proximates wave propagation in the subsurface and produces more reliable velocity updates than do
52 ray-based methods.

53 Wave-equation migration velocity analysis (Sava and Biondi, 2004a,b) is one variation of image-
54 domain wavefield tomography. The method linearizes the downward continuation operator and es-
55 tablishes a linear relationship between the model perturbation and image perturbation. The model
56 is inverted by exploiting this linear relationship and minimizing the image perturbation. Differen-
57 tial semblance optimization is another variation of image-domain wavefield tomography (Shen and
58 Symes, 2008). The idea is to minimize the difference of any given reflection between neighboring
59 offsets or angles by model updates. For differential semblance optimization, one important element
60 is the choice of the input image gathers. The theory is first introduced based on surface-offset gath-
61 ers (Symes and Carazzone, 1991). The concept is then generalized to space-lag (subsurface-offset)
62 (Shen and Calandra, 2005; Shen and Symes, 2008). Space-lag gathers have several advantages over
63 other types of gathers. First, space-lag gathers are obtained by wave-equation migration and have
64 fewer artifacts than usually found in surface-offset gathers obtained by Kirchhoff migration, and
65 thus they are suitable for velocity analysis in complex subsurface areas (Stolk and Symes, 2004).
66 Second, the implementation using space-lag gathers is automatic in a way that no moveout picking
67 is required, which significantly reduced the human interference.

68 In practice, however, the use of space-lag gathers is limited by the computation and storage
69 requirements. In 3D, space-lag gathers need to compute the lags in both inline and crossline di-
70 rections. This leads to 5D image hypercubes which are too expensive to compute and store. Clapp
71 (2007) proposed using FPGAs to accelerate the space-lag gathers construction. Compressed sensing

72 can also be used to reduce computation and storage cost, as proposed by Zhang et al. (2013). To
73 overcome the issues of space-lag gathers, we propose to use common-image-point gathers (CIPs)
74 as an alternative to space-lag gathers for image-domain wavefield tomography. The discrete sam-
75 pling of the point gathers provides a flexible way to extract the velocity information from the image
76 and facilitates target-oriented velocity updates. Furthermore, the sparse construction of the gathers
77 reduces computational cost and storage requirements, both are important in 3D applications. In ad-
78 dition, the algorithm used to pick the point gathers ensures that the gathers are sampled on reliable
79 reflection events. Other practical aspects regarding computational cost for image-domain wavefield
80 tomography fall outside the scope of this paper, e.g., I/O issue (Fei and Williamson, 2010).

81 We start the paper by introducing common-image-point gathers with focus on how to choose
82 the gather locations. We then discuss the theory of image-domain wavefield tomography and its
83 implementation with CIPs. Next, we introduce illumination weighting for the gathers aimed at
84 improving the robustness of the method. We use the Marmousi model to demonstrate that wavefield
85 tomography using sparsely sampled CIPs offers a more economical alternative to a conventional
86 approach using regularly sampled space-lag gathers for model building in complex subsurface areas.

THEORY

87 For clarity, we separate the theory section into three parts. We first discuss the picking algorithm to
88 sample CIPs in subsurface. We then explain the gradient computation for image-domain wavefield
89 tomography using CIPs. A synthetic example will be used to illustrate the flow as well. In the
90 third part, we explain the construction of the illumination-based weighting function which is used
91 to improve the robustness of the inversion.

92 **Gathers locations picking**

93 The essential and key characteristic of CIPs is the sparse sampling of gathers along reflections in
94 subsurface. In contrast, space-lag gathers used in conventional approach are sampled in the whole
95 subsurface. This full sampling of the gathers substantially increase the cost and may degrade the
96 gathers if they are sampled on noise or artifacts. The sampling locations for CIPs are determined
97 using an image-guided automatic algorithm(Cullison and Sava, 2011). The algorithm first computes
98 the image planarity, structure-oriented semblance, and the amplitude envelope; then use the multi-
99 plication of these three measures as the priority map to guide the location picking. The priority map
100 ensures that the gathers are sampled on coherent and continuous reflection events in subsurface. In
101 such a way, we achieve a robust characterization of the velocity information from the images. The
102 sparsity of the gathers construction is enforced by using exclusion zones. The exclusion zones can
103 be generated using structure tensor and the size of the zones is user-defined. The actual gathers
104 location is selected using a greedy heuristic picking method in the order of priority map value.

105 **Gradient computation**

106 For the image-domain wavefield tomography method discussed here, the objective function is for-
107 mulated by applying the idea of DSO to CIPs. The gradient is computed by applying the adjoint-
108 state method (Plessix, 2006; Symes, 2009),

109 For simplicity, we discuss the derivation in the frequency-domain. We formulate the inverse
110 problem by first defining the state variables, through which the objective function is related to the
111 model parameters. The state variables for our problem are the source and receiver wavefields u_s

112 and u_r obtained by solving the following acoustic wave equation:

$$\begin{bmatrix} \mathcal{L}(\mathbf{x}, \omega, m) & 0 \\ 0 & \mathcal{L}^*(\mathbf{x}, \omega, m) \end{bmatrix} \begin{bmatrix} u_s(j, \mathbf{x}, \omega) \\ u_r(j, \mathbf{x}, \omega) \end{bmatrix} = \begin{bmatrix} f_s(j, \mathbf{x}, \omega) \\ f_r(j, \mathbf{x}, \omega) \end{bmatrix}, \quad (1)$$

113 where f_s is the source function, f_r are the recorded data, $j = 1, \dots, N_s$, where N_s is the number of
 114 shots, ω is the angular frequency, and $\mathbf{x} = \{x, y, z\}$ are the space coordinates. The wave operator \mathcal{L}
 115 and its adjoint \mathcal{L}^* propagate the wavefields forward and backward in time, respectively, using either
 116 a one-way or two-way wave equation. In this formulation, we designate the operator \mathcal{L} to be

$$\mathcal{L} = -\omega^2 m - \Delta, \quad (2)$$

117 where Δ is the Laplace operator, and m represents slowness squared.

118 Figure 1(a) shows the synthetic model used to illustrate the flow. The true model consists of
 119 a Gaussian low-velocity anomaly in a constant background. A contrast at 1.6 km in the density
 120 model is used to generate the reflections. The initial model is the constant background, and the
 121 corresponding migrated image is shown in Figure 1(b). The imaged reflection is distorted due to the
 122 missing anomaly in the initial model.

123 In the second step of the adjoint-state method, we first construct the objective function. Then,
 124 the adjoint sources are derived based on the objective function, and used to model the adjoint-
 125 state variables. As the objective function measures the image incoherency caused by model error,
 126 minimizing the objective function simultaneously reconstructs the model and improves the image
 127 quality. The objective function for DSO is defined as:

$$\mathcal{H}_\lambda = \frac{1}{2} \|P(\lambda) r(\mathbf{x}, \lambda)\|_{\mathbf{x}, \lambda}^2, \quad (3)$$

128 where

$$r(\mathbf{x}, \boldsymbol{\lambda}) = \sum_j \sum_{\omega} \overline{u_s(j, \mathbf{x} - \boldsymbol{\lambda}, \omega)} u_r(j, \mathbf{x} + \boldsymbol{\lambda}, \omega) \quad (4)$$

129 the overline represents complex conjugate, and

$$P(\boldsymbol{\lambda}) = |\boldsymbol{\lambda}|, \quad (5)$$

130 The penalty operator annihilates the focused energy at zero lags and highlights the defocusing at
 131 non-zero lags.

132 For CIPs, Sava and Vasconcelos (2011) analyze the kinematic characteristics of reflections and
 133 point out that reflections focus at zero space- and time-lags when the migration velocity is correct.
 134 This feature is similar to that of space-lag gathers used in DSO. Therefore, we can define a DSO-
 135 type objective function for CIPs as

$$\mathcal{H}_{\boldsymbol{\lambda}, \tau} = \frac{1}{2} \|P(\boldsymbol{\lambda}, \tau) r(\mathbf{c}, \boldsymbol{\lambda}, \tau)\|_{\mathbf{x}, \boldsymbol{\lambda}, \tau}^2, \quad (6)$$

136 where $r(\mathbf{c}, \boldsymbol{\lambda}, \tau)$ are CIPs sampled on locations \mathbf{c} picked using the algorithm described in the pre-
 137 vious section:

$$r(\mathbf{c}, \boldsymbol{\lambda}, \tau) = \sum_j \sum_{\omega} \overline{u_s(j, \mathbf{c} - \boldsymbol{\lambda}, \omega)} u_r(j, \mathbf{c} + \boldsymbol{\lambda}, \omega) e^{2i\omega\tau} \quad (7)$$

138 $P(\boldsymbol{\lambda}, \tau)$ is

$$P(\boldsymbol{\lambda}, \tau) = \sqrt{|\boldsymbol{\lambda}|^2 + (V\tau)^2}, \quad (8)$$

139 where the space-lag vector $\boldsymbol{\lambda} = \{\lambda_x, \lambda_y, 0\}$, V is a constant scalar. Figure 2(a) and Figure 2(b)
 140 show two CIPs constructed in the middle of the reflector (Figure 1(b)) for true and initial models,
 141 respectively. The energy is focused in the gathers for the true model, and vice versa for the initial

142 model. The penalty operator is shown in Figure 2(c).

143 Given $\mathcal{H}_{\lambda, \tau}$ in equation 6, the adjoint sources are computed as objective function's derivatives
 144 with respect to the state variables u_s and u_r . To facilitate the derivation, we introduce an operator
 145 T which represents the space shift applied to the wavefields and is defined as

$$T(\boldsymbol{\lambda}) u(j, \mathbf{x}, \omega) = u(j, \mathbf{x} + \boldsymbol{\lambda}, \omega) , \quad (9)$$

146 Thus, the adjoint sources g_s and g_r are

$$\begin{aligned} g_s(j, \mathbf{x}, \omega) &= \sum_{\lambda, \tau} T(\boldsymbol{\lambda}) P(\boldsymbol{\lambda}, \tau) \overline{P(\boldsymbol{\lambda}, \tau) r(\mathbf{x}, \boldsymbol{\lambda}, \tau)} T(\boldsymbol{\lambda}) u_r(j, \mathbf{x}, \omega) e^{-2i\omega\tau} \\ g_r(j, \mathbf{x}, \omega) &= \sum_{\lambda, \tau} T(-\boldsymbol{\lambda}) P(\boldsymbol{\lambda}, \tau) \overline{P(\boldsymbol{\lambda}, \tau) r(\mathbf{x}, \boldsymbol{\lambda}, \tau)} T(-\boldsymbol{\lambda}) u_s(j, \mathbf{x}, \omega) e^{-2i\omega\tau} \end{aligned} \quad (10)$$

147 The adjoint state variables a_s and a_r are the wavefields obtained by backward and forward
 148 modeling respectively, using the corresponding adjoint sources defined in equation 10:

$$\begin{bmatrix} \mathcal{L}^*(\mathbf{x}, \omega, m) & 0 \\ 0 & \mathcal{L}(\mathbf{x}, \omega, m) \end{bmatrix} \begin{bmatrix} a_s(j, \mathbf{x}, \omega) \\ a_r(j, \mathbf{x}, \omega) \end{bmatrix} = \begin{bmatrix} g_s(j, \mathbf{x}, \omega) \\ g_r(j, \mathbf{x}, \omega) \end{bmatrix} , \quad (11)$$

149 and \mathcal{L} and \mathcal{L}^* are the same wave propagation operators used in equation 1.

150 The last step of the gradient computation is simply the correlation between state variables and
 151 adjoint state variables:

$$\begin{aligned} \frac{\partial \mathcal{H}_{\lambda, \tau}}{\partial m} &= \\ \sum_j \sum_{\omega} \frac{\partial \mathcal{L}}{\partial m} &\left(u_s(j, \mathbf{x}, \omega) \overline{a_s(j, \mathbf{x}, \omega)} + u_r(j, \mathbf{x}, \omega) \overline{a_r(j, \mathbf{x}, \omega)} \right) , \end{aligned} \quad (12)$$

152 where $\frac{\partial \mathcal{L}}{\partial m}$ is the partial derivative of the wave propagation operator with respect to the model pa-
153 rameter. Using the definition of \mathcal{L} in equation 2, we find that $\frac{\partial \mathcal{L}}{\partial m}$ is simply $-\omega^2$. Figure 3(a) shows
154 a gradient for one CIPs in the middle and computed from one shot at 1.5 km. The two branches
155 correspond to the source- and receiver-side crosscorrelation of the state and adjoint state variables.
156 The gradient for all CIPs and all shots stacked is shown in Figure 3(b), which characterizes the
157 Gaussian anomaly.

158 The derivation above shows the construction of objective function and gradient for image-
159 domain wavefield tomography. Given these two components, the solution to the inverse problem is
160 found by minimizing the objective function using non-linear gradient-based iterative methods. In
161 each iteration, the gradient is computed and the model update is calculated by line search in the
162 steepest descent or conjugate gradient directions (Vigh and Starr, 2008b). Using this flow, the up-
163 dated model after 10 iterations for the synthetic test is shown in Figure 4(a), where the Gaussian
164 anomaly is accurately reconstructed. The migrated image using the updated model is plotted in
165 Figure 4(b), where the image quality is improved.

166 **Illumination weighting**

167 The objective function $\mathcal{H}_{\lambda, \tau}$ defined in equation 6 is minimized when the reflections focus at zero
168 lag, an indication of the correct velocity model. This, however, occurs only when the subsurface is
169 well illuminated and the data has sufficient spatial sampling. Otherwise, imbalanced illumination or
170 irregular acquisition geometry can result in defocusing in the gathers even if the velocity model is
171 correct (Yang et al., 2012). To mitigate the negative influence of the uneven subsurface illumination,
172 we can employ a weighting function such that the gathers in poor illumination areas are down-
173 weighted as the defocusing information is less reliable than for the gathers in good illumination

174 areas. Such a weighting function stabilizes the inversion and improves the robustness of the model
 175 building process.

176 The weighting function is constructed using the illumination analysis. Illumination analysis
 177 in the framework of wave-equation migration is formulated using the solution to migration de-
 178 convolution problems (Yu and Schuster, 2003). Migration deconvolution first establishes a linear
 179 relationship between a reflectivity distribution \tilde{r} and seismic data d :

$$\mathcal{M}\tilde{r}(\mathbf{x}) = d, \quad (13)$$

180 where \mathcal{M} represents a forward Born modeling operator which is linear with respect to the reflec-
 181 tivity. A migrated image is obtained by applying the adjoint of the modeling operator \mathcal{M}^* to the
 182 data,

$$\mathcal{M}^*d = \mathcal{M}^*\mathcal{M}\tilde{r}(\mathbf{x}) = r(\mathbf{x}), \quad (14)$$

183 where r is a migrated image. Note that the migrated image is the result of blurring the reflectivity \tilde{r}
 184 by $(\mathcal{M}^*\mathcal{M})$. $(\mathcal{M}^*\mathcal{M})$ is the Gauss-Newton approximation to the Hessian of the least-squares misfit
 185 function, and it includes the subsurface illumination information associated with the velocity struc-
 186 ture and acquisition geometry. In practice, the matrix $(\mathcal{M}^*\mathcal{M})^{-1}$ is effectively noninvertible, but
 187 its impact can be evaluated by applying a cascade of demigration and migration operator $(\mathcal{M}^*\mathcal{M})$
 188 to an image:

$$r_I(\mathbf{x}) = \mathcal{M}^*\mathcal{M}r(\mathbf{x}), \quad (15)$$

189 The quotient $r_I(\mathbf{x})/r(\mathbf{x})$ approximates the diagonal elements of the Hessian and characterizes the
 190 illumination effects. This quotient is used as the illumination weighting function for our method.
 191 The weighting function is calculated using the initial velocity model. Although the model will be

192 updated during the inversion, we assume that the illumination is a slowly varying function with
193 respect to the model changes. As a result, the same illumination weighting is used to precondition
194 the gathers throughout the inversion.

EXAMPLES

195 In this section, we illustrate our method with synthetic Marmousi example to show its ability to
196 reconstruct velocity models in complex subsurface regions.

197 The correct model is shown in Figure 5(a). The source locations are evenly distributed on the
198 surface from 1.0 km to 7.0 km at a spacing of 0.1 km. The receiver arrays are fixed for all the
199 shots and span entirely the surface at a spacing of 0.01 km. The data are generated via finite-
200 difference Born modeling, using a Ricker wavelet with peak frequency of 15 Hz. The data are
201 then transformed into the frequency domain because both the migration and wavefield tomography
202 operators are based on the frequency-domain downward continuation method. In this way, we
203 avoid using the same operator for both the modeling and inversion procedures. The image and
204 angle gathers migrated with the true model are shown in Figures 5(b)-5(c). As one might expect,
205 reflections events in the angle gathers are flat because the correct model is used for migration.
206 The initial model used for the inversion, Figure 6(a), is a highly smoothed version of the true model.
207 This model resembles the results one can obtain from conventional ray-based reflection tomography.
208 Figures 6(b)-6(c) show the image and angle-domain CIGs migrated with the initial model. Since
209 the initial model is highly smoothed, it lacks the necessary components required by the migration
210 to produce an accurate result. Thus, the migrated image exhibits distortions in the reservoir region
211 around $x = 5$ km, $z = 2.5$ km. The reduced image quality can be further confirmed by the residual
212 moveout in the angle gathers, as shown in Figures 6(c). In our example, the angle gathers are used

213 only for quality control not the model building.

214 We initiate our velocity analysis process by selecting CIPs gather locations at which we con-
215 struct extended images necessary for velocity analysis. These locations are selected using the auto-
216 matic picking algorithm developed by Cullison and Sava (2011) as we discuss in the previous theory
217 section. Figure 6(b) shows the picked locations overlain on the image. They follow the coherent
218 structure of the image, and tend to be randomly positioned where the reflections are less coherent.
219 Figure 7 shows the weighting function obtained using equation 15. We apply it to the input gathers
220 in order to compensate for the uneven illumination effects in the subsurface. Light colors indicate
221 low values of the weights which correspond to the poor illumination areas, and dark colors indicate
222 high value of the weights which correspond to the good illumination areas. This weighting function
223 down weights the gathers in the poor illumination areas such that the inversion suffers less from the
224 unreliable information. Figures 8(a) and 8(b) show the inverted model after 20 nonlinear iterations
225 and the corresponding migrated image. The updated model improves the imaging quality in the
226 area ranges from $x = 4 \sim 6.5$ km, and from $z = 1 \sim 3$ km as the reservoir is better focused and
227 more coherent now. In addition, the reflections are flatter in angle gathers, as shown in Figure 8(c),
228 as compared with those in Figure 6(c). These also indicate the improvement of the image due to the
229 model updates.

DISCUSSION

230 The synthetic examples demonstrate the velocity model updates produced using CIPs. After running
231 the inversion, the main features of the model are resolved and they help improving the quality of
232 the image. The improvements can be directly observed from the more coherent image and flatter
233 events in angle gathers. In either case, CIPs are sparsely sampled along the reflectors but they

234 are still able to capture the velocity error and reconstruct the model. Compared to conventional
 235 DSO approach using space-lag gathers, the computation and storage cost for gathers is smaller. For
 236 space-lag gathers, the cost is proportional to the size of the model and number of lags we compute:
 237 $C \sim N_x N_y N_z N_{\lambda_x} N_{\lambda_y}$. For CIPs, the cost is proportional to the number of points and lags we
 238 compute: $C \sim N_c N_{\lambda_x} N_{\lambda_y} N_\tau$. Here N_c denotes the number of CIPs. Notice that the cost reduction
 239 is determined by the ratio $N_c N_\tau / (N_x N_y N_z)$. The number of time lag N_c is usually a small
 240 window which is only required to accommodate the wavelet. Thus the ratio of N_τ / N_z is generally
 241 less than 0.1. The ratio of $N_c / (N_x N_y)$ may depend on the complexity of the subsurface. Given the
 242 complex model like Marmousi model, we can still achieve the satisfied result using point gathers
 243 less than 1% of the total grid points. Another advantage of CIPs is that the gathers are always
 244 sampled on reflections as the picking is done using the greedy algorithm applied to the priority map.
 245 This improves the robustness of the gathers compared to space-lag gathers because the gathers suffer
 246 less from the noise or artifacts in the image.

CONCLUSIONS

247 We demonstrate a wavefield-based velocity model building method implemented in the image do-
 248 main. The procedure optimizes the velocity model by minimizing the image incoherency caused
 249 by model errors. The objective function is designed for common-image-point gathers constructed
 250 sparsely on the reflection event. The penalty operator used in the objective function is aimed at
 251 improving the focusing of the reflections in the gathers.

252 The synthetic examples demonstrate that CIPs are able to characterize velocity error from fo-
 253 cusing of the energy in the gathers, and the wavefield tomography converts the information into
 254 accurate velocity updates. The main advantages of using CIPs over conventional space-lag gathers

255 in the wavefield tomography approach is that using CIPs reduce the cost for computing and storing
256 the input image gathers while still produce reliable and accurate model updates. This is mainly
257 attributed to the optimized sampling of CIPs in the subsurface as only the significant reflections
258 are analyzed to provide information for velocity update. The illumination-based weighting helps
259 improve the stability and robustness of the inversion in complex subsurface areas.

ACKNOWLEDGMENTS

260 We acknowledge the support of the sponsors of the Center for Wave Phenomena at Colorado School
261 of Mines. The reproducible numeric examples in this paper use the Madagascar open-source soft-
262 ware package freely available from <http://www.reproducibility.org>. This research was supported
263 in part by the Golden Energy Computing Organization at the Colorado School of Mines using re-
264 sources acquired with financial assistance from the National Science Foundation and the National
265 Renewable Energy Laboratory.

REFERENCES

- 266 Al-Yahya, K., 1989, Velocity analysis by iterative profile migration: *Geophysics*, **54**, 718–729.
- 267 Clapp, R., 2007, Accelerating subsurface offset gathers for 3d seismic applications using fpgas:
268 77th Annual International Meeting, SEG, Expanded Abstracts, 2383–2387.
- 269 Cullison, T., and P. Sava, 2011, An image-guided method for automatically picking common-image-
270 point gathers: Presented at the 81th Annual International Meeting, SEG, Expanded Abstracts.
- 271 Etgen, J., S. H. Gray, and Y. Zhang, 2009, An overview of depth imaging in exploration geophysics:
272 *Geophysics*, **74**, WCA5–WCA17.
- 273 Fei, W., and P. Williamson, 2010, Overcoming the i/o bottleneck of adjoint state method based mi-
274 gration velocity analysis: 80th Annual International Meeting, SEG, Expanded Abstracts, 4057–
275 4061.
- 276 Gray, S. H., J. Etgen, J. Dellinger, and D. Whitmore, 2001, Seismic migration problems and solu-
277 tions: *Geophysics*, **66**, 1622–1640.
- 278 Plessix, R.-E., 2006, A review of the adjoint state method for computing the gradient of a functional
279 with geophysical applications: *Geophysical Journal International*, **167**, 495–503.
- 280 ———, 2009, Three-dimensional frequency-domain full-waveform inversion with an iterative
281 solver: *Geophysics*, **74**, WCC53–WCC61.
- 282 Pratt, R. G., 1999, Seismic waveform inversion in the frequency domain, Part 1: Theory and verifi-
283 cation in a physical scale model: *Geophysics*, **64**, 888–901.
- 284 Sava, P., and B. Biondi, 2004a, Wave-equation migration velocity analysis - I: Theory: *Geophysical*
285 *Prospecting*, **52**, 593–606.
- 286 ———, 2004b, Wave-equation migration velocity analysis - II: Subsalt imaging examples: *Geophys-*
287 *ical Prospecting*, **52**, 607–623.
- 288 Sava, P., and I. Vasconcelos, 2011, Extended imaging condition for wave-equation migration: *Geo-*

289 physical Prospecting, **59**, 35–55.

290 Shen, P., and H. Calandra, 2005, One-way waveform inversion within the framework of adjoint
291 state differential migration: 75th Annual International Meeting, SEG, Expanded Abstracts, 1709–
292 1712.

293 Shen, P., and W. W. Symes, 2008, Automatic velocity analysis via shot profile migration: Geo-
294 physics, **73**, VE49–VE59.

295 Sirgue, L., and R. Pratt, 2004, Efficient waveform inversion and imaging: A strategy for selecting
296 temporal frequencies: Geophysics, **69**, 231–248.

297 Stolk, C. C., and W. W. Symes, 2004, Kinematic artifacts in prestack depth migration: Geophysics,
298 **69**, 562–575.

299 Symes, W., 2009, Migration velocity analysis and waveform inversion: Geophysical Prospecting,
300 **56**, 765–790.

301 Symes, W. W., 2008, Migration velocity analysis and waveform inversion: Geophysical Prospect-
302 ing, **56**, 765–790.

303 Symes, W. W., and J. J. Carazzone, 1991, Velocity inversion by differential semblance optimization:
304 Geophysics, **56**, 654–663.

305 Tarantola, A., 1984, Inversion of seismic reflection data in the acoustic approximation: Geophysics,
306 **49**, 1259–1266.

307 Vigh, D., and E. W. Starr, 2008a, 3D prestack plane-wave, full-waveform inversion: Geophysics,
308 **73**, VE135–VE144.

309 ———, 2008b, Comparisons for waveform inversion, time domain or frequency domain?: 78th
310 Annual International Meeting, SEG, Expanded Abstracts, 1890–1894.

311 Virieux, J., and S. Operto, 2009, An overview of full-waveform inversion in exploration geophysics:
312 Geophysics, **74**, WCC1–WCC26.

313 Warner, M., A. Ratcliffe, T. Nangoo, J. Morgan, A. Umpleby, N. Shah, V. Vinje, I. Stekl, L. Guasch,
314 C. Win, G. Conroy, and A. Bertrand, 2013, Anisotropic 3d full-waveform inversion: *Geophysics*,
315 **78**, R59–R80.

316 Woodward, M., D. Nichols, O. Zdraveva, P. Whitfield, and T. Johns, 2008, A decade of tomography:
317 *Geophysics*, **73**, VE5–VE11.

318 Woodward, M. J., 1992, Wave-equation tomography: *Geophysics*, **57**, 15–26.

319 Yang, T., J. Shragge, and P. Sava, 2012, Illumination compensation for image-domain wavefield
320 tomography: Presented at the 74th Mtg., Abstracts, Eur. Assoc. Expl. Geophys.

321 Yu, J., and T. Schuster, 2003, Migration deconvolution vs. least squares migration: Presented at the
322 74th Annual International Meeting, SEG, Expanded Abstracts.

323 Zhang, Y., B. Biondi, and R. Clapp, 2013, Accelerating residual moveout based wave-equation
324 migration velocity analysis with compressed sensing: 83th Annual International Meeting, SEG,
325 Expanded Abstracts, 4744–4749.

LIST OF FIGURES

326 1 (a) The true slowness model. A horizontal interface at 1.6 km is placed in the density
327 model to generate reflections. (b) The migrated image obtained using the initial constant back-
328 ground model.

329 2 CIPs sampled at the middle of the reflector for (a) The true model and (b) the initial model.
330 (c) The penalty operator applied to the CIPs.

331 3 Gradient for (a) one shot located at 1.5 km and (b) all shots.

332 4 (a) The updated model after 10 iterations of inversion using CIPs. (b) The migrated image
333 obtained using the updated model.

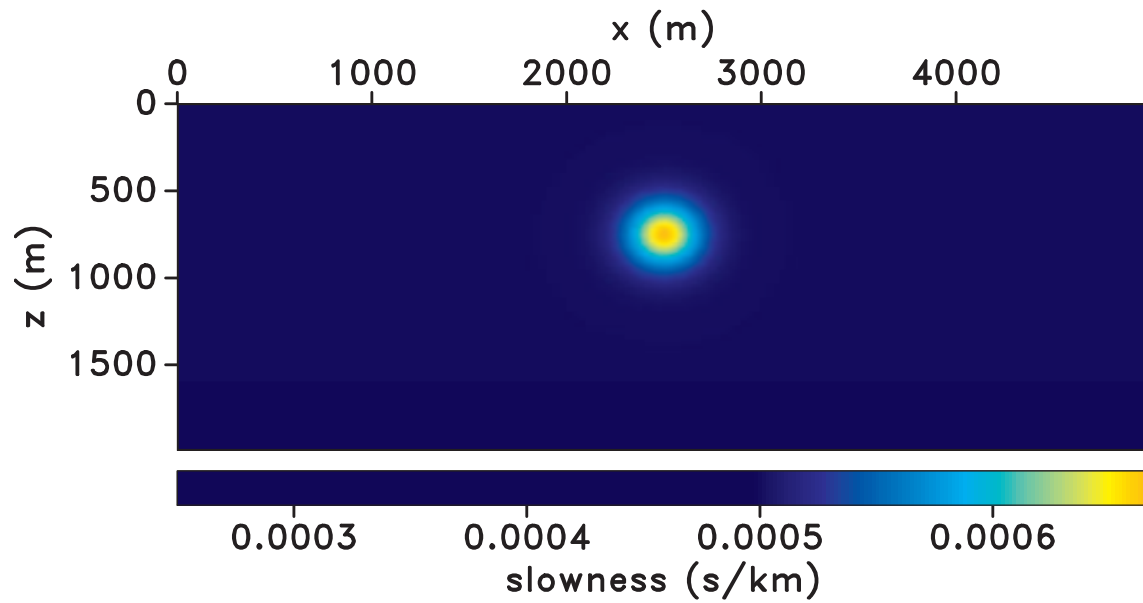
334 5 (a) The true model used to generate the data. (b) The migrated image overlain with the
335 CIPs location, and (c) the angle-domain gathers obtained using the true model.

336 6 (a) The initial model used in the velocity inversion. (b) The migrated image overlain with
337 the CIPs location, and (c) the angle-domain gathers obtained using the initial model.

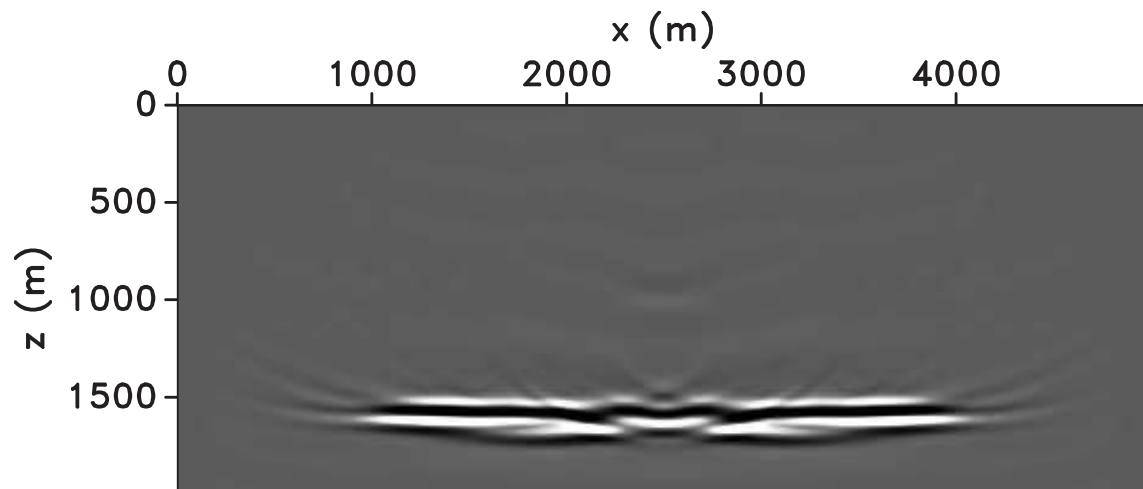
338 7 The weighting function based on the subsurface illumination.

339 8 (a) The updated model after 20 iterations of inversion using CIPs. (b) The migrated im-
340 age overlain with the CIPs locations, and (c) the angle-domain gathers obtained using the updated
341 model.

342



(a)



(b)

Figure 1: (a) The true slowness model. A horizontal interface at 1.6 km is placed in the density model to generate reflections. (b) The migrated image obtained using the initial constant background model.

-

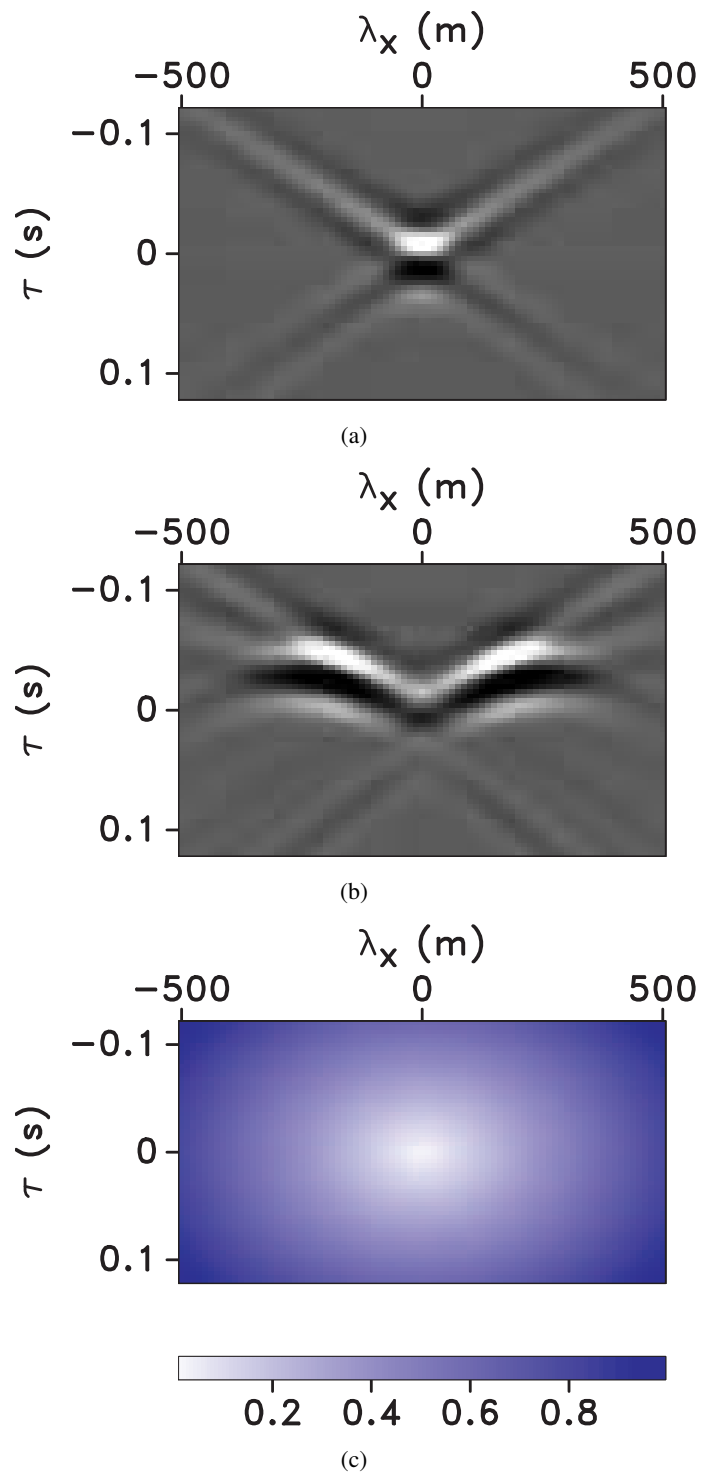
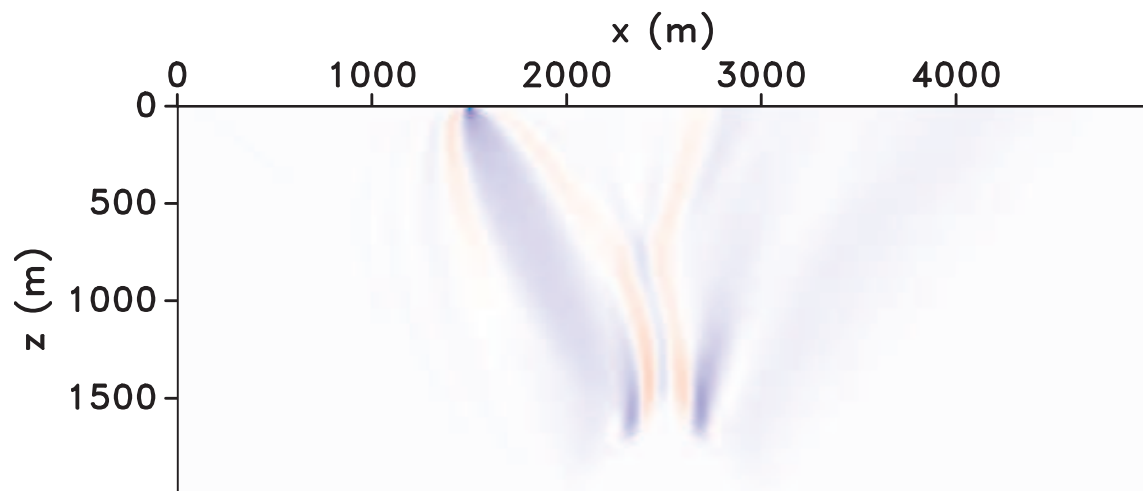
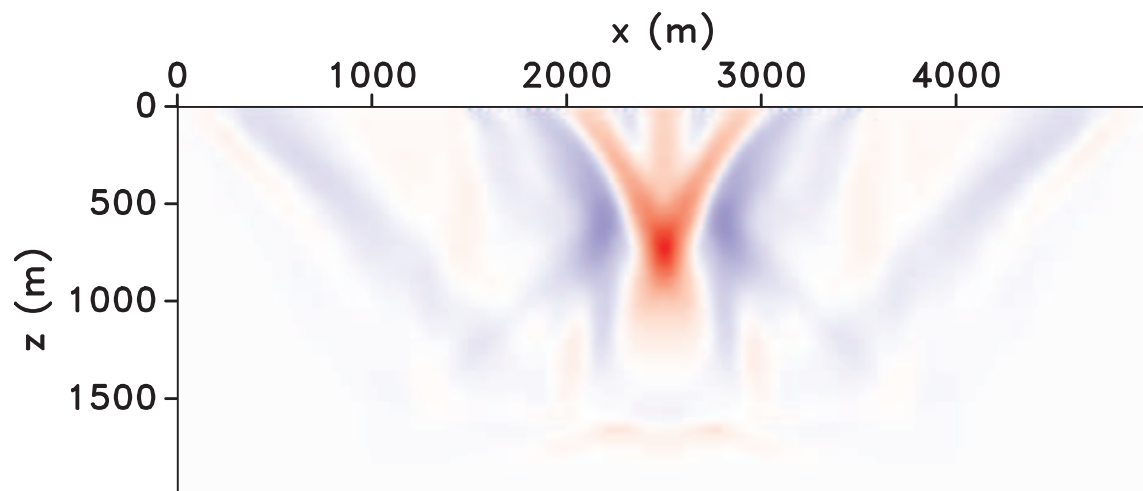


Figure 2: CIPs sampled at the middle of the reflector for (a) The true model and (b) the initial model. (c) The penalty operator applied to the CIPs.

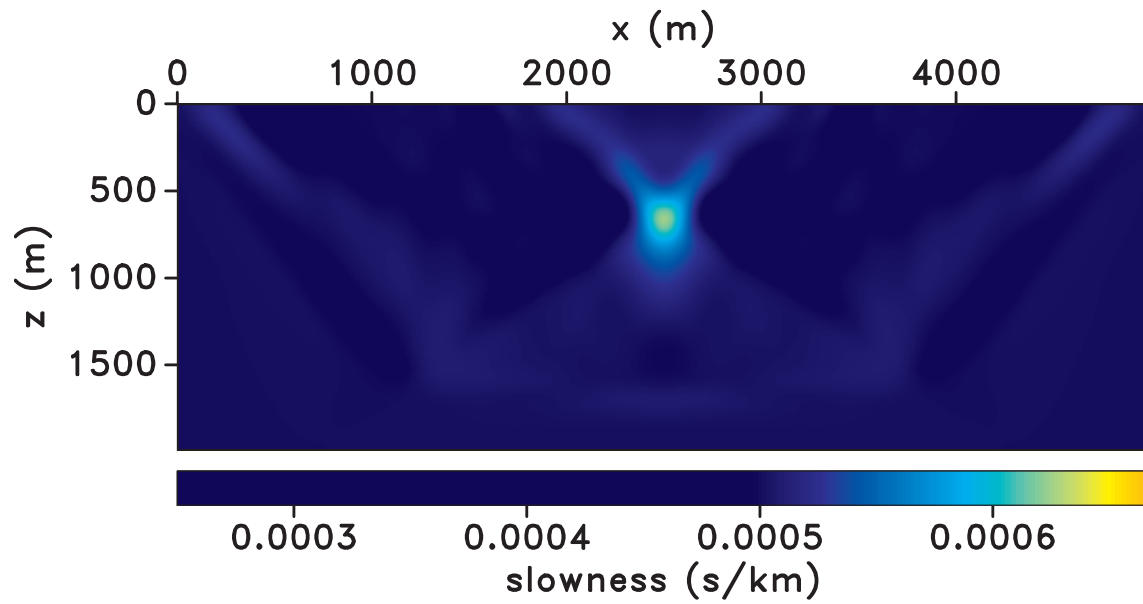


(a)

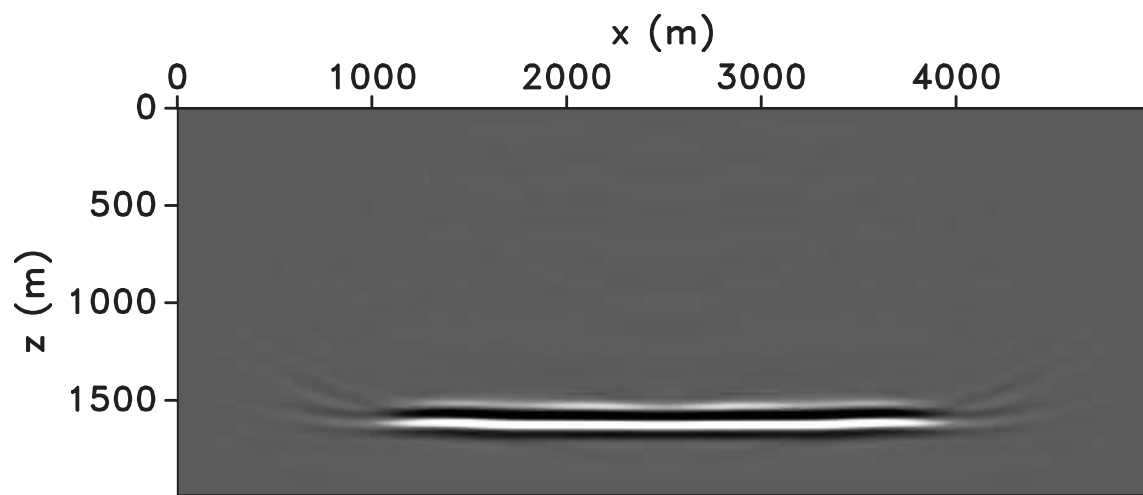


(b)

Figure 3: Gradient for (a) one shot located at 1.5 km and (b) all shots. –



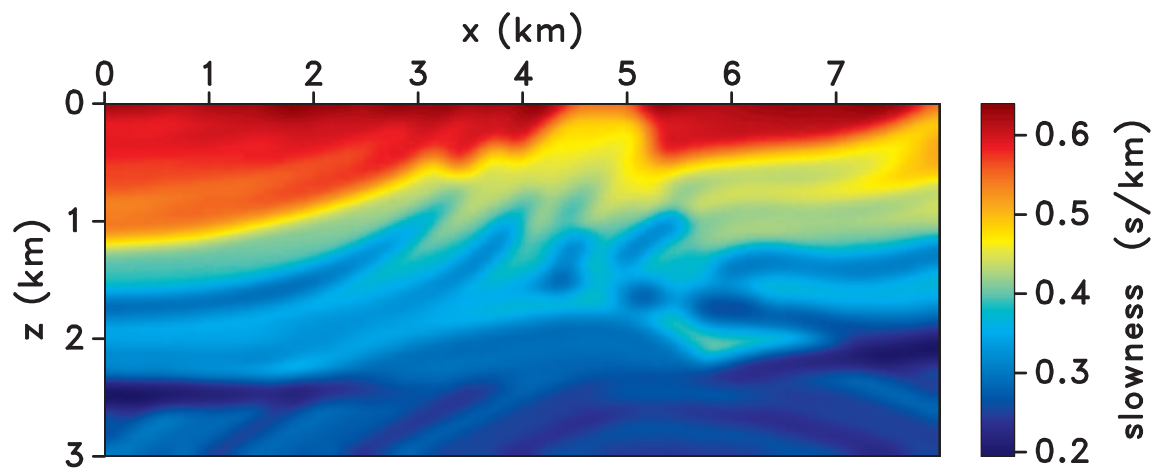
(a)



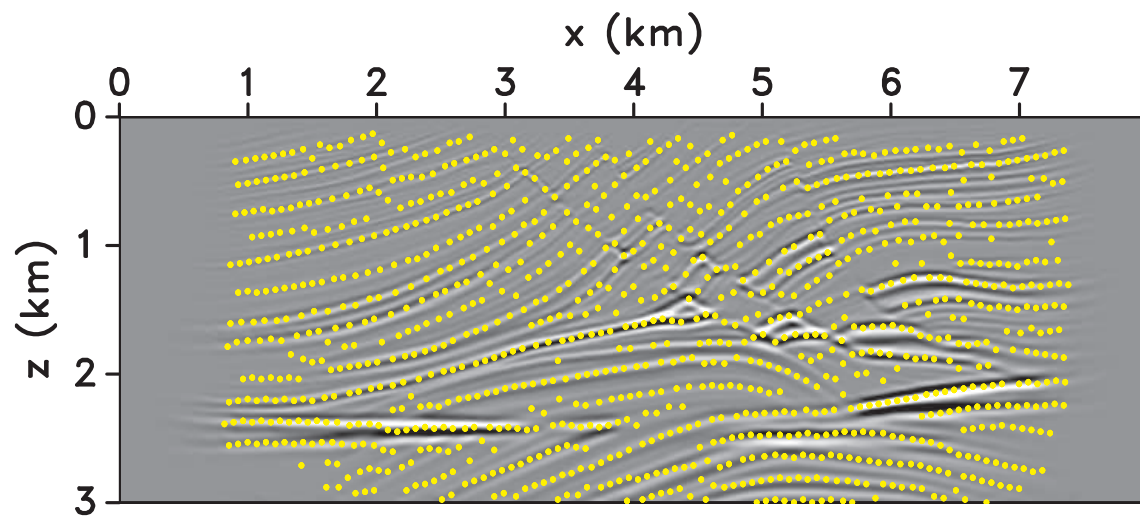
(b)

Figure 4: (a) The updated model after 10 iterations of inversion using CIPs. (b) The migrated image obtained using the updated model.

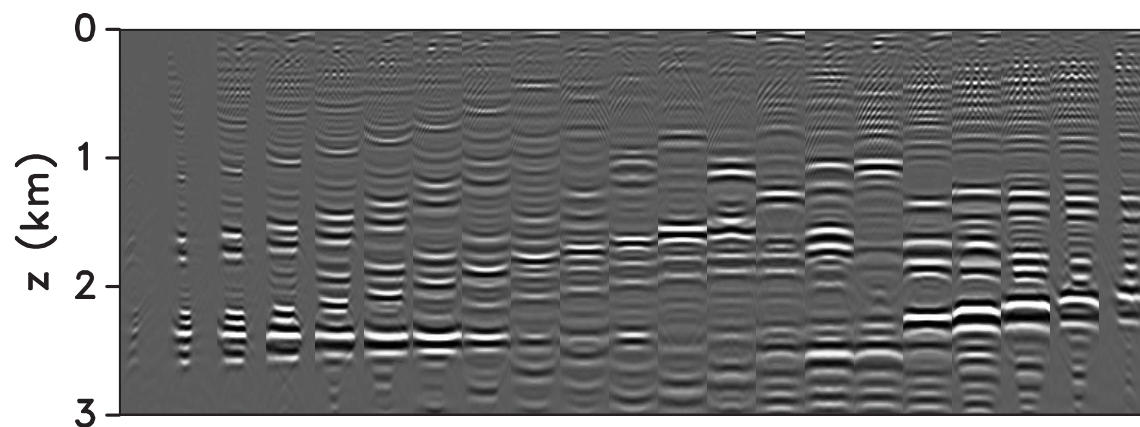
-



(a)

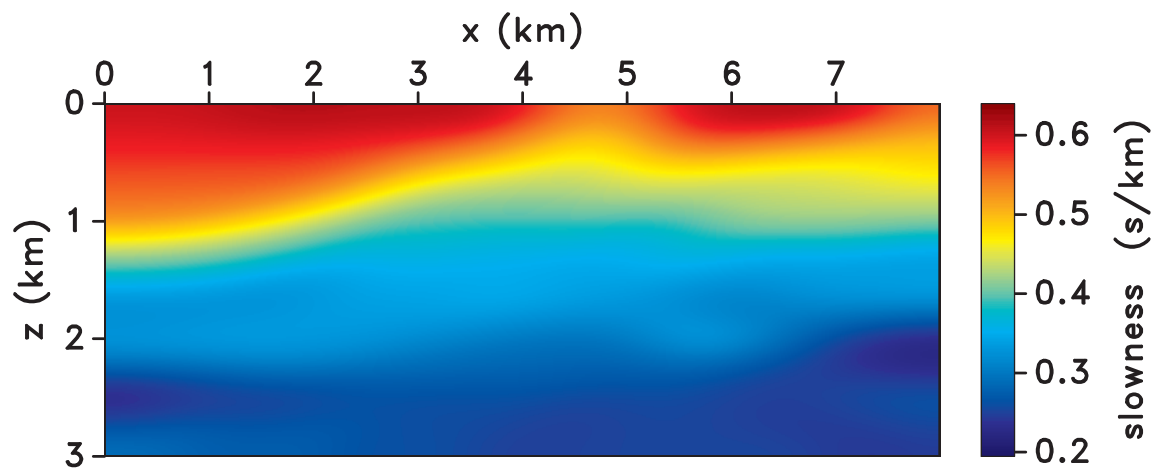


(b)

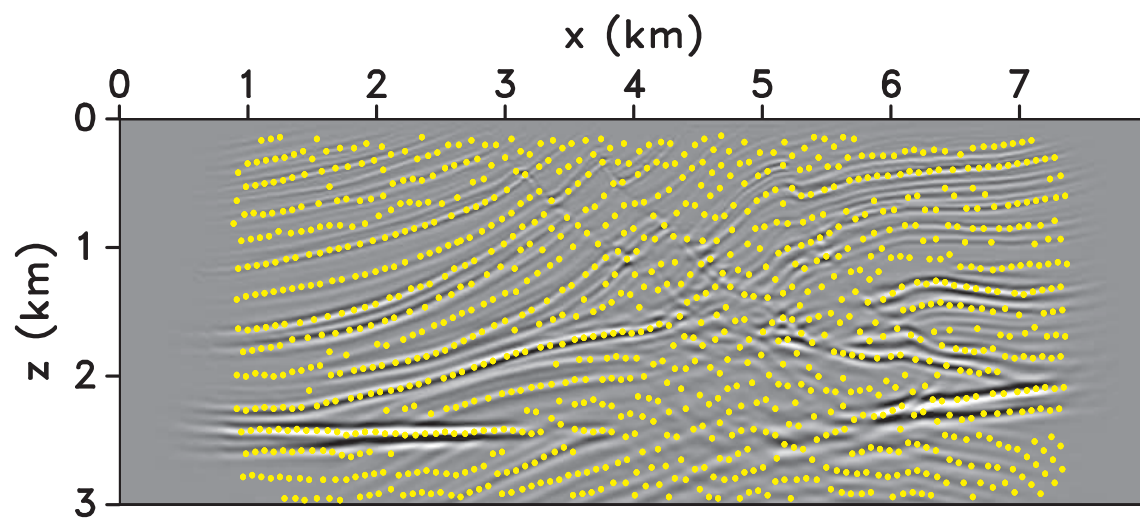


(c)

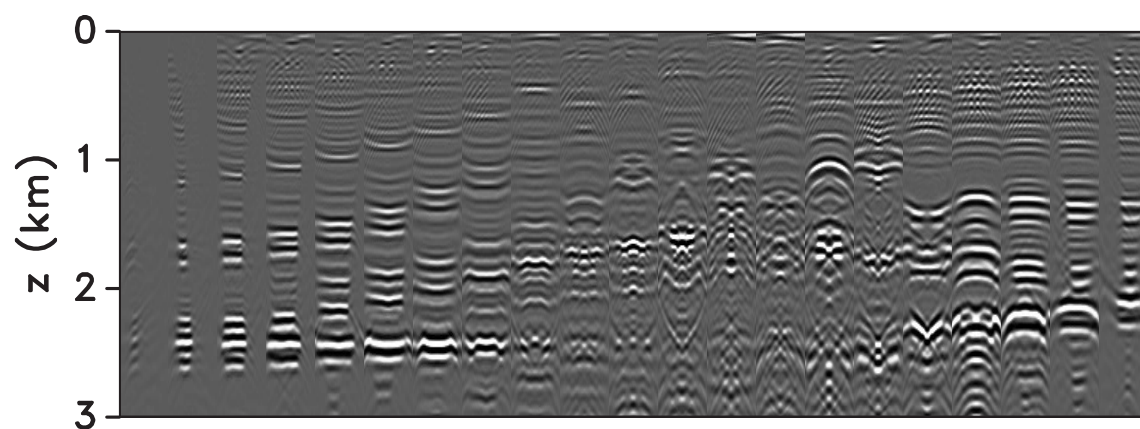
Figure 5: (a) The true model used to generate the data. (b) The migrated image overlain with the CIPs location, and (c) the angle-domain gathers obtained using the true model.



(a)



(b)



(c)

Figure 6: (a) The initial model used in the velocity inversion. (b) The migrated image overlain with the CIPs location, and (c) the angle-domain gathers obtained using the initial model.

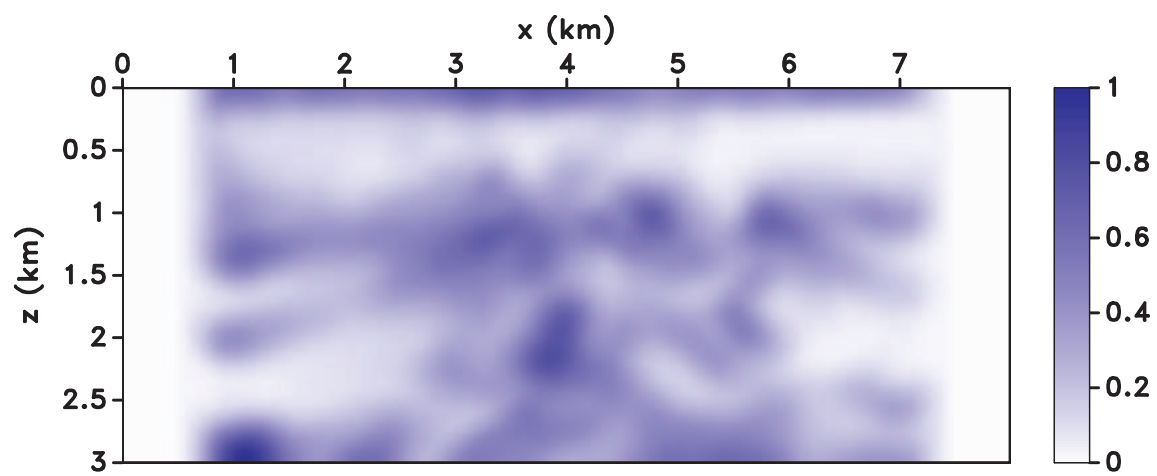
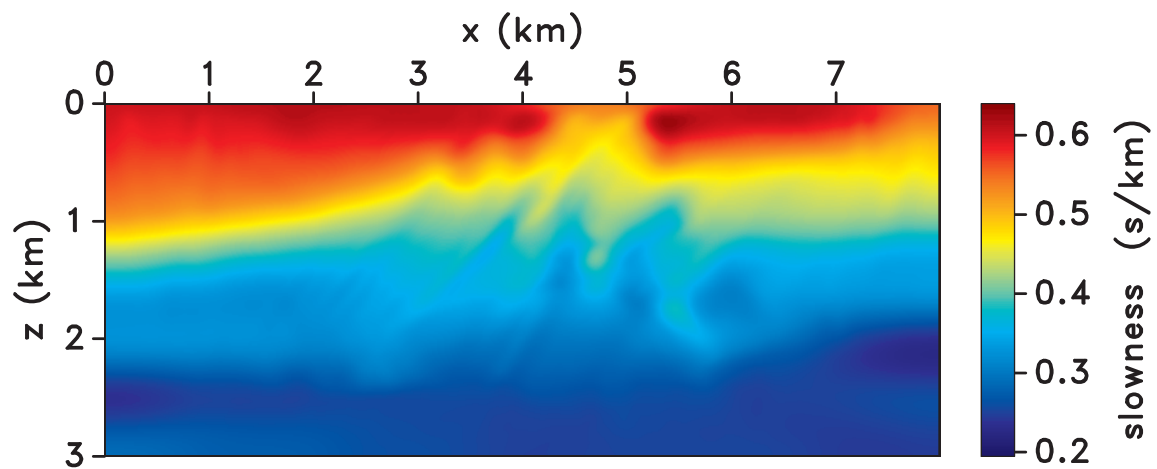
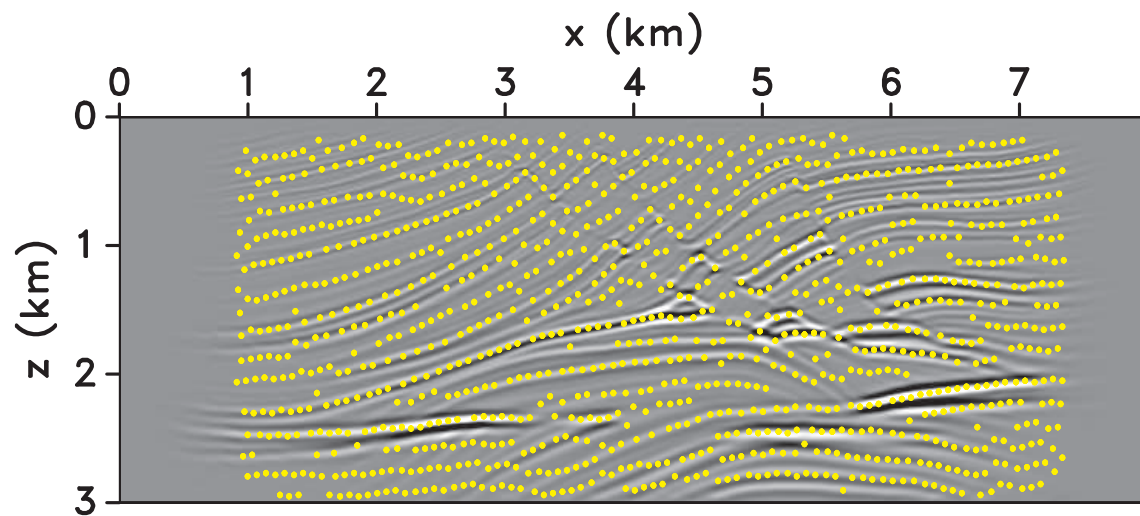


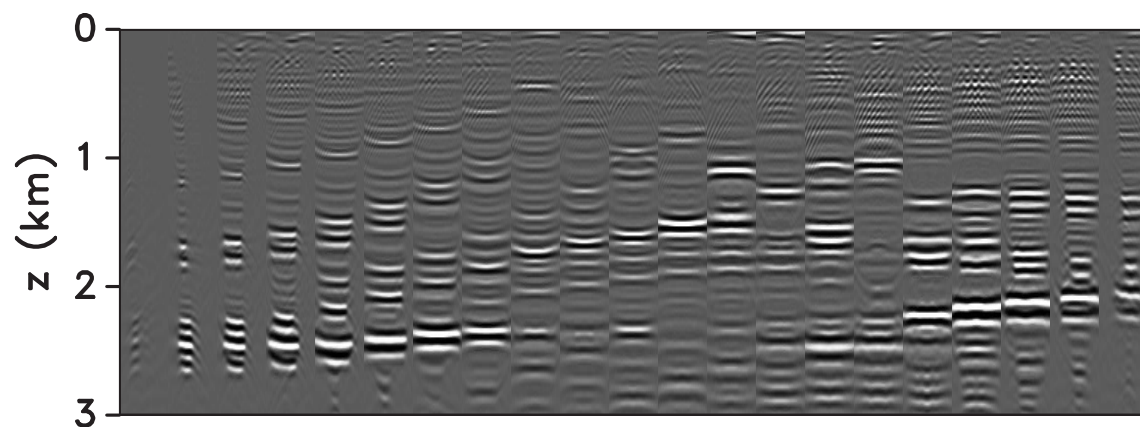
Figure 7: The weighting function based on the subsurface illumination. –



(a)



(b)



(c)

Figure 8: (a) The updated model after 20 iterations of inversion using CIPs. (b) The migrated image overlain with the CIPs locations, and (c) the angle-domain gathers obtained using the updated model.